LETTERS
https://doi.org/10.1038/s41563-021-00972-x

nature materials

Check for updates

Nonlinear valley phonon scattering under the strong coupling regime

Xiaoze Liu[1,2,6], Jun Yi[1,3,6], Sui Yang[1], Erh-Chen Lin[4], Yue-Jiao Zhang[3], Peiyao Zhang[1], Jian-Feng Li[3], Yuan Wang[1], Yi-Hsien Lee[4], Zhong-Qun Tian[3] and Xiang Zhang[1,5]✉

Research efforts of cavity quantum electrodynamics have focused on the manipulation of matter hybridized with photons under the strong coupling regime[1–3]. This has led to striking discoveries including polariton condensation[2] and single-photon nonlinearity[3], where the phonon scattering plays a critical role[1–9]. However, resolving the phonon scattering remains challenging for its non-radiative complexity. Here we demonstrate nonlinear phonon scattering in monolayer MoS_2 that is strongly coupled to a plasmonic cavity mode. By hybridizing excitons and cavity photons, the phonon scattering is equipped with valley degree of freedom and boosted with superlinear enhancement to a stimulated regime, as revealed by Raman spectroscopy and our theoretical model. The valley polarization is drastically enhanced and sustained throughout the stimulated regime, suggesting a coherent scattering process enabled by the strong coupling. Our findings clarify the feasibility of valley–cavity-based systems for lighting, imaging, optical information processing and manipulating quantum correlations in cavity quantum electrodynamics[2,3,10–17].

The part-light, part-matter quasiparticles called cavity polaritons are formed under the strong coupling regime where the coupling rate is faster than the decay rates of light and matter. The manipulation of matter with light in cavity quantum electrodynamics has been a major research focus for photonic applications and quantum materials[1–3]. Unprecedented material properties through the hybridization of light and matter lead to intriguing phenomena such as polariton condensation[2] and single-photon nonlinearity[3]. Convoluted with overwhelming fluorescence actions in cavities[1–3], the hidden non-radiative phonon scattering via ubiquitous lattice-displacement and light coupling plays a critical role in the physical behaviours of cavity polaritons[1–7]. For example, it plays one of the dominant roles in the non-radiative damping that is critical for polariton condensation[1,2,4], enhances the quantum correlation of emitters in cavities[3,5,6] and even enables the possibility of light-induced high-transition-temperature (high T_C) superconductivity[8,9]. Under the strong coupling regime, the phonon scattering could also be fundamentally altered and thus suggest distinct underlying mechanisms of cavity polaritons. However, resolving the phonon scattering has been challenging for the complexity of its non-radiative nature. In this work, we demonstrate the nonlinear valley phonon scattering in monolayer MoS_2 under the strong coupling regime.

The strong coupling system is based on a plasmonic cavity embedded with monolayer MoS_2. The superb capability of plasmonic structures to concentrate light into deep-subwavelength volumes dramatically enables the strong coupling regime into the atomic monolayer limit[18] and single-molecule level[19]. Monolayer transition metal dichalcogenide (TMD) MoS_2 is selected here for three reasons: first, the large oscillator strength in the monolayer limit ensures the strong coupling regime[20]; second, the rich valley physics in monolayer TMDs provides a new valley degree of freedom (DOF) and valley selection rule to investigate the phonon scattering[21,22]; and third, the typical phonon scattering in monolayer TMDs can be directly probed using Raman spectroscopy[21,23]. Under the strong coupling regime of such a cavity system, hybrid quasiparticles of plasmon-cavity exciton polaritons (PEPs, also known as plexcitons) are formed. When the phonon scattering is probed via Raman spectroscopy, the exciton constituent of PEPs introduces valley phonon scattering behaviours corresponding to strong valley electron–phonon interactions[21,23,24], while the plasmon cavity constituent enhances phonon modes by the factor of $|E_p/E_0|^4$ (E_p/E_0 is the electric field ratio of the plasmon field E_p to free space field E_0) and can even induce stimulated phonon scattering[25,26]. The unique hybrid nature of the phonon scattering results from the synergy of the exciton resonance and plasmonic enhancement of the polaritonic states. Rather than only the Raman intensity enhancement seen in other strong coupling systems[27,28], the phonon scattering reveals coherent valley scattering behaviours: it breaks down the classical Raman selection rule and drastically enhances valley polarization by 2.5 times, which is non-degradable throughout the stimulated regime. These findings provide a practical route towards the valleytronics in demand for the coupled valley–cavity systems[10–14]. They also directly lead to explorations of more specific phonons under the strong coupling regime, such as longitudinal optical phonons with unique chirality[15] and Fröhlich interactions[16] for quantum coherence and entanglement[3,5,6].

The sample structure and experimental configuration are illustrated in the schematic of Fig. 1. The plasmon cavity structure with the TMD monolayer is shown in Fig. 1b. The cavity samples are composed of core–shell structured nanospheres (Supplementary Fig. 1) and a chemical vapour deposition (CVD) MoS_2 monolayer film on a gold (Au) substrate (Supplementary Fig. 2). The Au substrate consists of a 3 nm Al_2O_3 film and 200 nm Au film on a SiO_2/Si substrate. More details of sample preparation are discussed in the Methods. The electric field distribution of the highly compact plasmon cavity mode is simulated as in Supplementary Fig. 3a, ensuring efficient coupling with TMD excitons. New PEP states (Fig. 1a) are formed by the strong coupling between TMD valley excitons and a plasmon cavity mode. The PEP states here

[1]NSF Nanoscale Science and Engineering Center, University of California, Berkeley, CA, USA. [2]School of Physics and Technology, Wuhan University, Wuhan, China. [3]State Key Laboratory of Physical Chemistry of Solid Surfaces, College of Chemistry and Chemical Engineering, Xiamen University, Xiamen, China. [4]Department of Materials Science and Engineering, National Tsing-Hua University, Hsinchu, Taiwan, Republic of China. [5]Faculty of Science and Faculty of Engineering, The University of Hong Kong, Hong Kong, China. [6]These authors contributed equally: Xiaoze Liu, Jun Yi. ✉e-mail: president@hku.hk

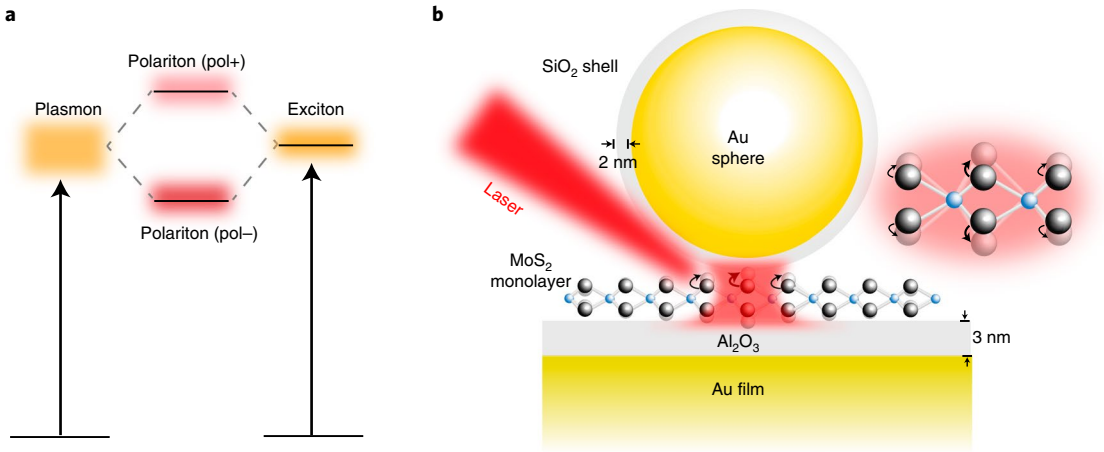

Fig. 1 | Schematics of demonstrating phonon scattering under the strong coupling regime. a, Energy diagram of the PEP states (pol+ and pol– are the upper and lower polaritons, respectively) that originate from strong coupling between the plasmonic cavity mode and excitons in monolayer MoS_2. **b**, Illustration of the sample structures. Core–shell structured nanospheres on gold substrate with an Al_2O_3 spacer layer form compact plasmonic cavities. Transferred monolayer MoS_2 is sandwiched inside a plasmonic cavity where the strong coupling regime is reached. The highly confined electric field in such a cavity ensures efficient coupling with MoS_2 excitons. When PEPs are generated via resonant pump, the phonon scattering behaviours (sketched intuitively as arrows) are found to be determined by the hybrid properties of PEPs.

involve strong phonon scatterings, including Raman-active phonon modes[21,23,24,29] (lattice vibrations) and silent phonon modes[21,23]. To clarify the phonon scattering processes, the strong coupling regime is first characterized, and the phonon modes are then investigated via PEP-resonant Raman spectroscopy.

Strong coupling between monolayer excitons and plasmon cavity modes is determined via dark-field scattering spectroscopy. The exciton A energy of monolayer MoS_2 is identified as ~665 nm (~1.865 eV) and as the dashed line in the differential reflectivity spectrum of Fig. 2a, which is resonant with the plasmon cavity mode. Due to the highly confined in-plane electric field component efficiently coupled to exciton dipoles of monolayer MoS_2 (Supplementary Fig. 3), the dark-field scattering spectrum features two split peaks separated by ~130 meV (Fig. 2a), indicating the strong coupling between the plasmon cavity mode and exciton A. To characterize the strong coupling regime, the dark-field spectra are taken for plasmon cavities with various detunings ($\delta = E_{plm} - E_{ex}$) ranging from positive through negative values. These detunings are realized by varying the size of gold nanospheres with a measured fundamental mode (control experiment in Supplementary Fig. 5). In Fig. 2b, nine typical dark-field spectra are selected, as the plasmon cavity modes are progressively varied across the exciton A energy. Two prominent split modes at both sides of the exciton (dashed line) vary the peak intensities and positions. From negative to positive detunings (spectra from top to bottom), the intensity of the lower-energy (longer-wavelength) mode becomes weaker, and the peak approaches the exciton line but never crosses it, and vice versa for the other mode. With two red curves as the guidelines, the strong coupling regime is evidenced by the anticrossing feature of these two modes. In addition, the simulation of these spectra is also carried out (Supplementary Fig. 3c) and consistent with the experiment. The dispersion data of PEPs based on tens of samples are summarized in Fig. 2c, and are well fitted with a coupled-oscillator model for a Rabi splitting of 130 ± 6 meV (Methods). The strong coupling is verified by comparing this splitting with the linewidths of the plasmon and exciton (Methods), and is further confirmed by the photoluminescence (PL) features (Fig. 2a).

The phonon scattering processes under the strong coupling regime are then directly probed by polarization-resolved Raman spectroscopy. For demonstration purposes, we focus on three phonon modes: the E′, A_1' and 2LA(K) modes. For monolayer MoS_2, the Raman-active E′ and A_1' modes are two of the most prominent phonons, representing the in-plane and out-of-plane lattice vibrations, respectively (Fig. 3a)[21,23,24,29]. The silent mode 2LA(K) is round-trip intervalley scattering between the K and K′ valleys by two longitudinal acoustic LA(K) phonons with wavevectors $\mathbf{q} \sim \mathbf{K}$ and $\mathbf{q} \sim -\mathbf{K}$ (Fig. 3b), which is strongly correlated with valley polarization and can be activated by the resonance pump condition through the double resonance Raman (DRR) process[21,23]. To better resolve the phonon scattering, the Raman spectroscopy is carried out at 77 K at different conditions (Fig. 3c and Supplementary Figs 6–9). In Fig. 3c, the measured Raman spectra are categorized into three sets of plasmon-enhanced, exciton-resonant and polariton-resonant spectra. For the plasmon-enhanced condition (plasmon case), the pump laser at an off-resonance wavelength of 532 nm is applied to a monolayer MoS_2 plasmonic cavity with resonance peaked at 555 nm, which is not coupled to MoS_2 excitons (Fig. 3c bottom spectra). The observed E′ (388 cm^{-1}) and A_1' (408 cm^{-1}) modes both show enhanced intensities with the same polarization selection rule in comparison with that on a Si/SiO_2 substrate (Supplementary Figs. 6 and 7). For the exciton-resonant condition (exciton case), the Raman spectra are taken under on-resonance excitation (633 nm) at 77 K for bare monolayer MoS_2 without a cavity (Fig. 3c middle spectra). The Raman intensities for E′ and A_1' are much weaker than in the plasmon case, and the Raman-silent mode 2LA(K) emerges around 460 cm^{-1}. All the Raman modes have shown valley polarization dependence. For the polariton-resonant condition (polariton case), Raman spectra are taken on a monolayer MoS_2 plasmonic cavity at 77 K by on-resonance excitation of 633 nm (Fig. 3b top spectra). Interestingly, all of the E′, A_1' and 2LA(K) modes have amplified intensities and strong valley polarization dependence.

In the plasmon case, the coupling between circular polarization and Raman modes is determined by the transverse/longitudinal nature of specific modes. For example, the transverse mode E′ could rotate the linear polarization by 90° with respect to the linearly polarized pump light, while the longitudinal A_1' could preserve the linear polarization without change[23,26,29]. For the circularly polarized pump, E′ could flip the handedness and A_1' could preserve it[23,26,29]. The polarization selection rule could be further understood by

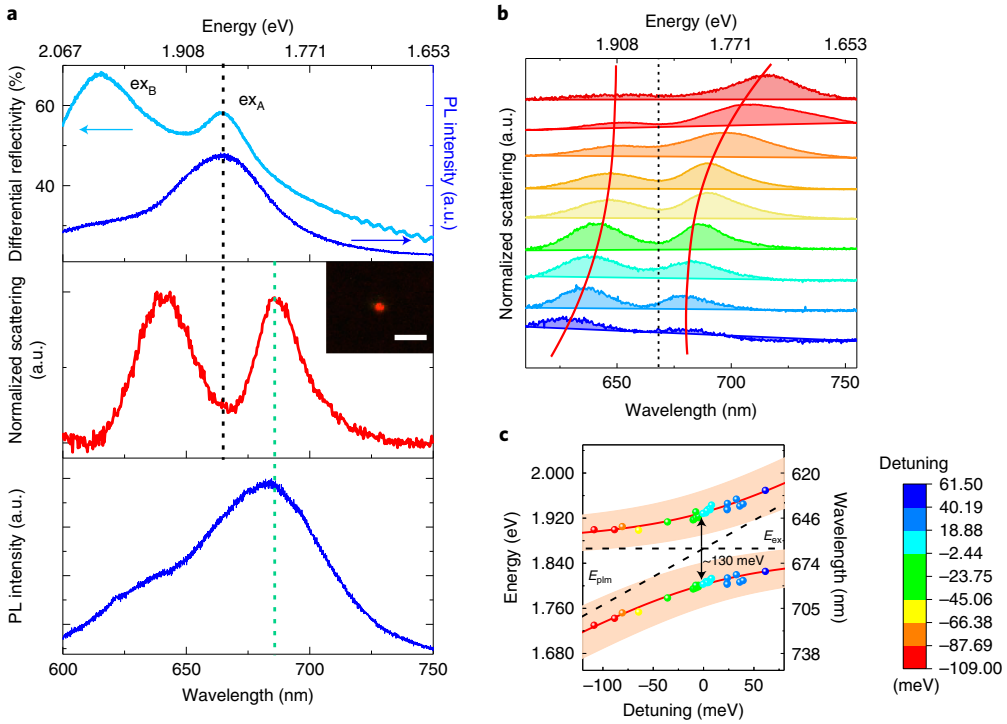

Fig. 2 | Determination of the strong coupling regime in a MoS_2 monolayer embedded in plasmonic cavities. a, Upper panel: for the monolayer MoS_2 on a silicon substrate, the differential reflectivity spectrum shows the energies of excitons B and A (ex_B and ex_A); the PL shows a dominant peak for ex_A. Middle panel: normalized dark-field scattering spectrum of a plasmonic cavity with monolayer MoS_2 shows two polariton peaks. Dark-field image of the nanosphere is shown in the inset with a 2 μm scale bar. Lower panel: the corresponding PL spectrum of the cavity sample in the middle panel. The main peak, ~680 nm, corresponds to the lower polariton state. This spectrum consists of dominant PL emissions of the plasmonic cavity and a very small portion of uncoupled ex_A emission (Supplementary Figure 4). The black dashed line labels the ex_A energy, and the green dashed line labels the lower polariton energy. **b**, Measured dark-field scattering spectra of nine typical cavity samples with monolayer MoS_2 at various detunings ($\delta = E_{plm} - E_{ex}$). Black dashed line labels ex_A energy. Two prominent split modes lie on both sides of ex_A. Red curves are guidelines indicating two anticrossed modes. **c**, PEP dispersion. The coloured dots are experimental spectral peaks representing the polariton modes, where the colour bar represents the detuning. A coupled-oscillator model is carried out to fit the polariton branches. The model demonstrates a Rabi splitting of 130 ± 6 meV for the strong coupling regime.

classical Raman theory (Methods)[23,29]. In addition, the Raman intensity enhanced by plasmon I_p scales as $I_p \propto I_0 |E_p/E_0|^4$ (I_0 is the intensity without plasmonic enhancement). This polarization selection rule only works for off-exciton-resonance pump scenarios.

In the exciton and polariton cases, the coupling between circular polarization and Raman modes mainly involves valley exciton resonances, instead of coming from optical excitations (Supplementary Fig. 10). When the pump laser is resonant with excitons, the intensity (I_{ex}) follows quantum theory[21,23],

$$I_{ex} \propto \Gamma_{g\to ex}\Gamma_{e-ph}\Gamma_{ex\to g} \quad (1)$$

where the $\Gamma_{g\to ex}$ and $\Gamma_{ex\to g}$ represent optical transitions (excitation and relaxation) between the ground state (g) and excitonic states (ex), and Γ_{e-ph} represents the electron–phonon interactions (Supplementary Note 1). In addition, due to valley exciton transitions (Supplementary Fig. 8), the coupling of opposite circular polarization for the E′ mode would be changed to the enhanced coupling of the same circular polarization. All the phonon scattering (Raman intensity) is also enhanced, and especially the silent modes based on electron–phonon interactions (Γ_{e-ph}) may also be activated. For the polariton case, the Raman modes would follow the quantum theory of the resonance scenario (exciton constituent) but be amplified by strong field confinements (plasmon constituent). The Raman modes thus follow,

$$I_{PEP} \propto \Gamma_{g\to pol+}\Gamma_{e-ph}\Gamma_{pol-\to g}|E_{PEP}/E_0|^4 \quad (2)$$

involving the optical transitions between ground state (g) and polaritonic states (pol±). Here I_{PEP} and E_{PEP} represent the Raman intensity and the electric field in the polariton case, respectively.

The observation in Fig. 3c can be understood for the strong coupling of valley excitons. In the plasmon case, the Raman scattering process is enhanced only by plasmons, as in $I_p \propto I_0 |E_p/E_0|^4$, following the Raman selection rule (Supplementary Fig. 6). The E′ mode is observed in the opposite circular polarization with the pump, and A_1' shows the same polarization with the pump[23,24,29]. Due to the smaller enhancement in the exciton case, E′ and A_1' are much weaker than in the plasmon case, while they show the same circular polarization with the pump laser. This dependence is mainly determined by the valley selection rule, following the $\Gamma_{g\to ex}$ and $\Gamma_{ex\to g}$ terms through the DRR process[24,29]. The activation of non-zero **q** mode 2LA(K) leads to the intensity of the exciton DRR process (I_{DRR-ex}) as[21],

$$I_{DRR-ex} \propto \Gamma_{g\to ex_1'}\Gamma_{e-2LA}\Gamma_{ex\to g} \quad (3)$$

This equation is similar to equation (2). The ex_1' and ex represent the excited exciton state (first pumped intermediate state) and final exciton state (radiation state), respectively; and Γ_{e-2LA} represents the unique 2LA(K) phonon scattering mediated by an intermediate exciton state ex_2' (Fig. 3b and Supplementary Note 1). The activation of 2LA(K) helps preserve the valley polarization of the excitons by competing with other depolarization scattering processes[22].

In the polariton case, the 2LA(K) mode is also activated by polariton resonances and dramatically enhanced by the plasmon

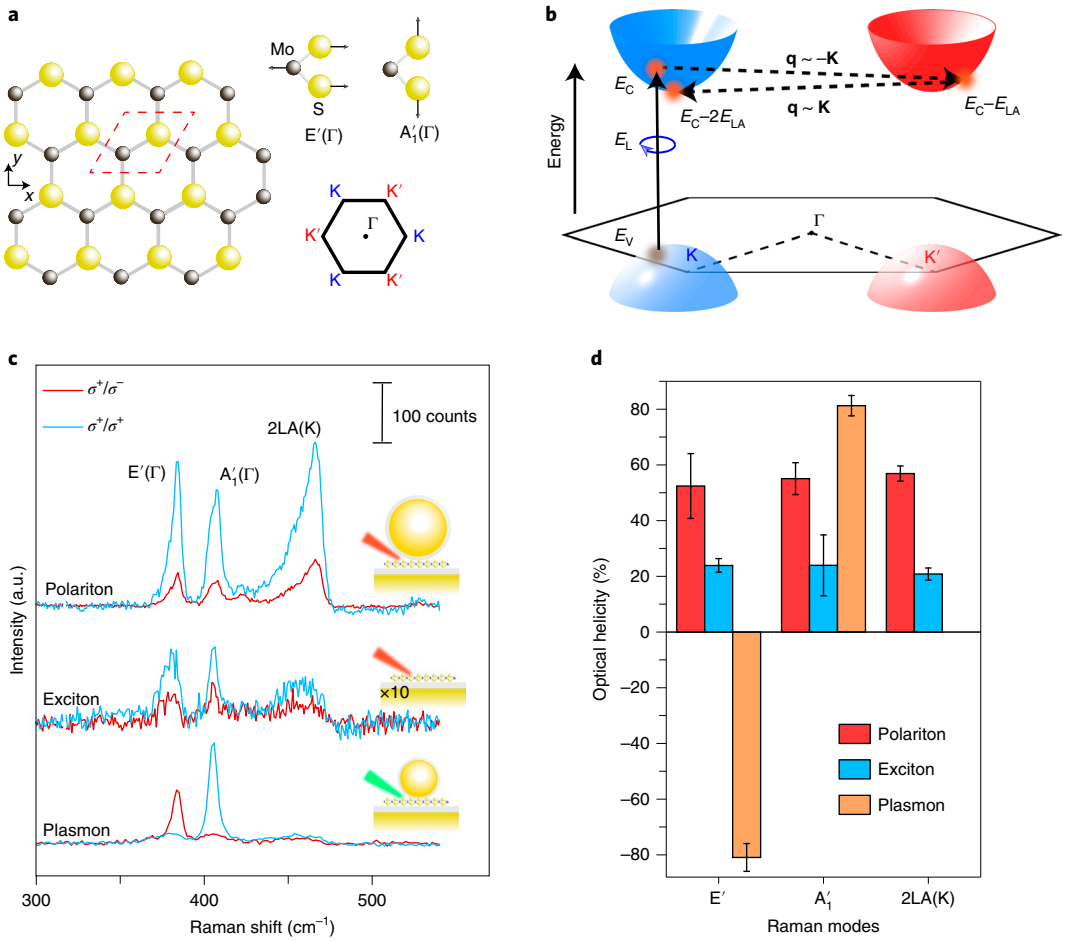

Fig. 3 | Direct observation of phonon scattering under the strong coupling regime. a, Typical phonon modes in monolayer MoS_2 including the Raman-active modes of E′ and A_1' phonons. Left panel shows top view of structures of monolayer MoS_2 and right panel shows the atomic vibrations for the E′ and A_1' mode at the Γ point of the Brillouin zone. **b**, Intervalley scattering of 2LA(K). It is a round-trip scattering between the K and K′ valleys by two longitudinal acoustic LA(K) phonons with wavevectors $\mathbf{q} \sim \mathbf{K}$ and $\mathbf{q} \sim -\mathbf{K}$. Here E_C, E_V, E_L, and E_{LA} refer to energies of conduction band, valence band, pump laser and LA(K) phonon, respectively. **c**, Polarization-resolved Raman spectra of monolayer MoS_2 under the strong coupling regime at 77 K. All spectra are for left circularly polarized σ^+ laser excitation with copolarized (blue curves) and cross-polarized (red curves) Raman, vice versa for right circularly polarized σ^- excitation (not shown here). For the plasmon case (bottom) with a blue-detuned cavity (plasmon resonance, ~555 nm), Raman modes are excited by an off-resonance continuous-wave laser (532 nm). For the exciton case (middle), where the cavity is absent, the Raman modes are excited by an on-resonance continuous-wave laser (633 nm). The intensity is multiplied by ten times for clarity. For the polariton case (top), where the exciton is strongly coupled with the cavity mode, Raman modes are excited with a 633 nm continuous-wave laser. The Raman peaks at 388 cm^{-1} and 408 cm^{-1} are assigned as the E′ and A_1' modes. The peak around 460 cm^{-1}, assigned as the 2LA(K) phonons, is visible in both the polariton and exciton cases, but only dramatically enhanced in the polariton case. These modes demonstrate distinctive optical helicity and large enhancements dictated by PEPs. **d**, Summarized histogram of optical helicity for the Raman modes in the three cases. The error bars are standard errors from multiple measurements. The polariton case follows the valley selection rule with enhanced helicity.

constituent of polaritons for the intensity of the PEP DRR process ($I_{DRR-PEP}$) as,

$$I_{DRR-PEP} \propto \Gamma_{g\to pol+}\Gamma_{e-2LA}\Gamma_{pol-\to g}|E_{PEP}/E_0|^4 \quad (4)$$

Here Γ_{e-2LA} represents 2LA(K) phonon scattering mediated by an intermediate polariton state pol'_+ (Supplementary Note 1). The DRR resonances are very different here: the outcoming photons could be resonant with the lower polariton state, while the incoming photons are resonant with the upper polariton state. This intensity dependence indicates orders of magnitude enhancement of 2LA(K) in the polariton case, which means dominant round-trip intervalley scattering over other processes of depolarization to further preserve the valley DOF. This microscopic picture reveals a distinct dark side from the fluorescence properties of valley-polarized polaritons in the strong coupling regime[10–14], and directly leads to our observation of helicity as summarized in Fig. 3d. The plasmon case shows almost perfect helicity of the E′ and A_1' modes determined by the Raman tensors. The exciton case demonstrates valley-dependent helicity of all the observed modes. The polariton case takes major features from both aforementioned cases: Raman modes follow the valley selection rule and demonstrate enhanced helicity by 2.5 times. The valley selection rule and enhanced Raman modes indicate facilitated valley-dependent phonon scattering by the hybrid nature of PEPs.

The PEP resonance effect also elicits stimulated phonon scattering under the strong coupling regime, evidenced by the superlinear feature of pump–power dependence. Similar to the set-up in power-dependent Raman measurements[25], the pulsed laser has an 80 MHz repetition rate, and is set to centre at 633 nm and

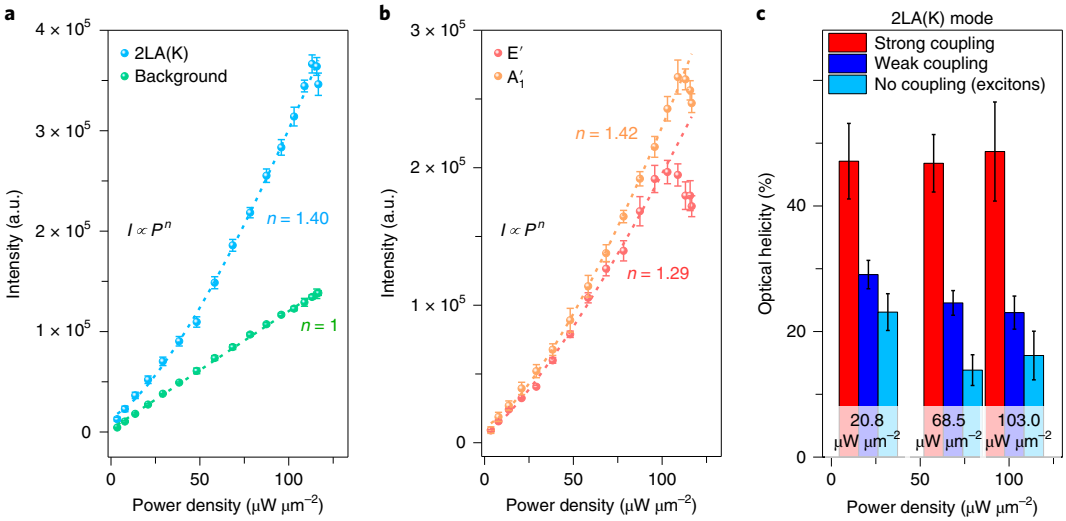

Fig. 4 | Uncovering stimulated phonon scattering by polariton-resonance excitation. a, Pump–power dependence of the integrated intensity of 2LA(K) modes (blue dots) and the fluorescence background (green dots, linear). **b**, Raman-active modes of E′ and A_1' phonons. The phonon modes are excited at 77 K by a pulsed laser. The error bars in **a** and **b** are standard errors from multiple measurements. The dashed lines illustrate the nonlinear fitting of power-law curves with power index *n*, before they reach the parametric instability regime where the Raman intensity starts to decrease. Only at this resonance case do all the Raman modes reach the superlinear regime with power index $n > 1$, indicating stimulated phonon scattering under the strong coupling regime. **c**, The pump–power dependence of the optical helicity of the 2LA(K) mode for strong coupling (polariton), weak coupling (Supplementary Figure 16 for details) and no coupling (exciton) cases are summarized at three typical powers: 20.8 μW μm^{-2}, 68.5 μW μm^{-2} and 103.0 μW μm^{-2}. In the polariton case, the optical helicity does not significantly drop at higher pump power, indicating that the particle-density-dependent exchange interaction barely affects the valley dynamics.

filtered into a linewidth of 0.7 nm (~15 cm^{-1}). The pump laser is resonant with polariton modes at 77 K and results in a consistent Raman shift with the continuous-wave resonance pump case (Supplementary Fig. 11). The power dependence of all the Raman modes shows superlinear dependence in Fig. 4, which is independent from the linear PL background. By fitting the power-law equation ($I \propto P^n$, where *I* is the intensity and *P* is the power density), the power index *n* is always greater than 1 for the E′, A_1' and 2LA(K) modes, indicating stimulated Raman scattering[25,26,30]. The nonlinear phonon scattering is modelled and generalized in a DRR scenario (Supplementary Note 2 and Supplementary Fig. 12) and would disappear at off-resonance pump cases (Supplementary Fig. 9). Because of further enhancement of the 2LA(K) phonon scattering, the optical valley helicity of the Raman modes remains unchanged in the nonlinear regime without influence by the strong polariton–polariton interaction through excitonic exchange interaction (Fig. 4c and Supplementary Fig. 13). The nonlinear power dependence persists until the intensity drops at the maximum power due to the parametric instability regime[25,26] without any sample damage (Supplementary Fig. 14). Moreover, this power dependence is largely affected by the cavity detuning (Supplementary Fig. 15), and is the most prominent on the resonance of the close-to-zero detuning cases. The valley-dependent stimulated scattering phenomenon thus provides a direct picture for the intervalley scattering and non-radiative relaxation processes. It is also worth noting that the weak coupling regime cannot lead to this observation. The control experiments (Fig. 4c and Supplementary Fig. 16) and simulation (Supplementary Fig. 17) of the weak coupling case clarify the fundamental difference between strong coupling and weak coupling for this scenario. This PEP resonance case represents a new degree of freedom for the nonlinear process of valley phonons, such as shifting the cavity detuning, varying the coupling strength and tuning the pump wavelength[26].

In summary, stimulated valley phonon scattering by the strong coupling regime is demonstrated in plasmonic cavities embedded with monolayer TMD. The polariton-resonant Raman spectroscopy reveals hybrid properties of electron–phonon interactions such as strong valley dependence and optical nonlinearity. This demonstration influences the exploration of more specific phonons[15,16] under the strong coupling regime and valley polariton condensation in two-dimensional materials[20]. For instance, the chiral longitudinal optical phonons can also be further studied for intervalley scattering via Fröhlich interactions, and for valley coherence and quantum entanglement in the framework of cavity quantum electrodynamics[3,6], when the quantum emitters of two-dimensional materials are coupled to a similar cavity configuration[17]. This work also suggests possibilities to directly study complex quantum behaviours for practical quantum applications in computing and communications[2,3].

Online content

Any methods, additional references, Nature Research reporting summaries, source data, extended data, supplementary information, acknowledgements, peer review information; details of author contributions and competing interests; and statements of data and code availability are available at https://doi.org/10.1038/s41563-021-00972-x.

Received: 18 February 2020; Accepted: 1 March 2021;
Published online: 12 April 2021

References

1. Sanvitto, D. & Kéna-Cohen, S. The road towards polaritonic devices. *Nat. Mater.* **15**, 1061–1073 (2016).
2. Deng, H., Haug, H. & Yamamoto, Y. Exciton-polariton Bose-Einstein condensation. *Rev. Mod. Phys.* **82**, 1489–1537 (2010).
3. Lodahl, P., Mahmoodian, S. & Stobbe, S. Interfacing single photons and single quantum dots with photonic nanostructures. *Rev. Mod. Phys.* **87**, 347–400 (2015).
4. Kasprzak, J., Solnyshkov, D. D., André, R., Dang, L. S. & Malpuech, G. Formation of an exciton polariton condensate: thermodynamic versus kinetic regimes. *Phys. Rev. Lett.* **101**, 146404 (2008).

5. Müller, K. et al. Ultrafast polariton-phonon dynamics of strongly coupled quantum dot-nanocavity systems. *Phys. Rev. X* **5**, 031006 (2015).
6. Seidelmann, T. et al. Phonon-induced enhancement of photon entanglement in quantum dot-cavity systems. *Phys. Rev. Lett.* **123**, 137401 (2019).
7. Gonzalez-Ballestero, C., Feist, J., Gonzalo Badía, E., Moreno, E. & Garcia-Vidal, F. J. Uncoupled dark states can inherit polaritonic properties. *Phys. Rev. Lett.* **117**, 156402 (2016).
8. Skopelitis, P., Cherotchenko, E. D., Kavokin, A. V. & Posazhennikova, A. Interplay of phonon and exciton-mediated superconductivity in hybrid semiconductor-superconductor structures. *Phys. Rev. Lett.* **120**, 107001 (2018).
9. Thomas, A. et al. Exploring superconductivity under strong coupling with the vacuum electromagnetic field. Preprint at https://arxiv.org/abs/1911.01459 (2019).
10. Chen, Y.-J., Cain, J. D., Stanev, T. K., Dravid, V. P. & Stern, N. P. Valley-polarized exciton-polaritons in a monolayer semiconductor. *Nat. Photon.* **11**, 431–435 (2017).
11. Dufferwiel, S. et al. Valley addressable exciton-polaritons in atomically thin semiconductors. *Nat. Photon.* **11**, 497–501 (2017).
12. Sun, Z. et al. Optical control of room-temperature valley polaritons. *Nat. Photon.* **11**, 491–496 (2017).
13. Chervy, T. et al. Room temperature chiral coupling of valley excitons with spin-momentum locked surface plasmons. *ACS Photon.* **5**, 1281–1287 (2018).
14. Lundt, N. et al. Optical valley Hall effect for highly valley-coherent exciton-polaritons in an atomically thin semiconductor. *Nat. Nanotechnol.* **14**, 770–775 (2019).
15. Zhu, H. et al. Observation of chiral phonons. *Science* **359**, 579–582 (2018).
16. Miller, B. et al. Tuning the Fröhlich exciton-phonon scattering in monolayer MoS_2. *Nat. Commun.* **10**, 807 (2019).
17. Luo, Y. et al. Deterministic coupling of site-controlled quantum emitters in monolayer WSe_2 to plasmonic nanocavities. *Nat. Nanotechnol.* **13**, 1137–1142 (2018).
18. Liu, W. et al. Strong exciton–plasmon coupling in MoS_2 coupled with plasmonic lattice. *Nano Lett.* **16**, 1262–1269 (2016).
19. Chikkaraddy, R. et al. Single-molecule strong coupling at room temperature in plasmonic nanocavities. *Nature* **535**, 127–130 (2016).
20. Mak, K. F. & Shan, J. Photonics and optoelectronics of 2D semiconductor transition metal dichalcogenides. *Nat. Photon.* **10**, 216–226 (2016).
21. Carvalho, B. R. et al. Intervalley scattering by acoustic phonons in two-dimensional MoS_2 revealed by double-resonance Raman spectroscopy. *Nat. Commun.* **8**, 14670 (2017).
22. Xu, X., Yao, W., Xiao, D. & Heinz, T. Spin and pseudospins in layered transition metal dichalcogenides. *Nat. Phys.* **10**, 343–350 (2014).
23. Zhang, X. et al. Phonon and Raman scattering of two-dimensional transition metal dichalcogenides from monolayer, multilayer to bulk material. *Chem. Soc. Rev.* **44**, 2757–2785 (2015).
24. Drapcho, S. G. et al. Apparent breakdown of Raman selection rule at valley exciton resonances in monolayer MoS_2. *Phys. Rev. B* **95**, 165417 (2017).
25. Lombardi, A. et al. Pulsed molecular optomechanics in plasmonic nanocavities: from nonlinear vibrational instabilities to bond-breaking. *Phys. Rev. X* **8**, 011016 (2018).
26. Schmidt, M. K., Esteban, R., González-Tudela, A., Giedke, G. & Aizpurua, J. Quantum mechanical description of Raman scattering from molecules in plasmonic cavities. *ACS Nano* **10**, 6291–6298 (2016).
27. Fainstein, A. & Jusserand, B. Cavity-polariton mediated resonant Raman scattering. *Phys. Rev. Lett.* **78**, 1576–1579 (1997).
28. Shalabney, A. et al. Enhanced Raman scattering from vibro-polariton hybrid states. *Angew. Chem. Int. Ed.* **54**, 7971–7975 (2015).
29. Chen, S.-Y., Zheng, C., Fuhrer, M. S. & Yan, J. Helicity resolved Raman scattering of MoS_2, $MoSe_2$, WS_2 and WSe_2 atomic layers. *Nano Lett.* **15**, 2526–2532 (2015).
30. Zhang, R. et al. Chemical mapping of a single molecule by plasmon-enhanced Raman scattering. *Nature* **498**, 82–86 (2013).

Methods

Sample preparation. Silica shell-isolated gold nanoparticles (SHINs) are chemically synthesized following a reported procedure[31]. Au nanoparticles are first synthesized based on a seeded growth method. Briefly, to prepare the seed solution first, 200 ml of chloroauric acid (0.01 wt%) is added into a flask and heated to boiling. Then 2 ml of sodium citrate (1 wt%) is quickly added into the boiling solution. The solution is kept boiling for 30 min and then cooled as seeds. To synthesize gold nanoparticles, 3 ml Au seed solution and 20 ml water are added into a flask, and ascorbic acid (1 wt%) and sodium citrate (1 wt%) are then added. The mixture is stirred in an ice bath. Chloroauric acid (0.825 wt%) is dropped in by a step motor. The synthesis of gold particles is accomplished by keeping the solution in a water bath at 70 °C for 15 min. The amount of ascorbic acid, sodium citrate and chloroauric acid are adjusted to control the average size of the particles, which determines the resonance wavelength of the plasmonic cavities, as listed in Supplementary Table 1. To synthesize the SHINs, the prepared Au nanoparticle solution is placed in a flask under stirring. Then 0.4 ml of 1 mM (3-aminopropyl) trimethoxysilane solution is added and stirred for 15 min. Then 3.2 ml of 0.54% sodium silicate solution is added to the flask. After stirring overnight at room temperature, the Au@SiO_2 SHINs with a shell of ~2 nm thickness are obtained.

The substrate is a continuous Au film covered by a thin layer of Al_2O_3, where the 200-nm-thick Au film is grown by electron beam evaporation (Edwards Vacuum, FC-2000) and the 3 nm Al_2O_3 is prepared by atomic layer deposition (Picosun Oy R-200 Advanced). The monolayer MoS_2 is synthesized at 650 °C by ambient pressure CVD using perylene-3,4,9,10-tetracarboxylic acid tetra-potassium salt as the seed on a SiO_2/Si substrate. Sulfur powder and molybdenum oxide (MoO_3) are used as precursors for the synthesis. The MoS_2 monolayer is then immersed in deionized water and lifted off from the substrate into water. The Al_2O_3/gold substrate is then used to 'fish out' the MoS_2 film. The SHIN particle solution is directly dropped onto the substrate and then dried under vacuum conditions with a vacuum desiccator.

The SHINs are characterized by transmission electron microscopy (TEM, JEM-2100) and bright-field and dark-field microscopy, as shown in Supplementary Figs. 1 and 2, respectively. The TEM images confirm uniform particles with an average core size of around 150 nm and shell thickness of 2 nm. Due to the strong light scattering of these particles, the formed plasmonic cavities can be identified via a dark-field microscope, which shows individual bright red dots in the image, indicating the resonances of cavities around 620–700 nm. The MoS_2 monolayer sample is characterized by PL (Horiba Labram HR Evolution) and differential reflectivity spectrum, as shown in Fig. 2 and Supplementary Fig. 4. The features are in good agreement with previous studies, indicating the exciton A resonance around 1.865 eV (665 nm).

Optical measurement. The scattering spectroscopy of individual plasmonic cavities is measured via a home-built confocal set-up, shown in Supplementary Fig. 18a. White light from a halogen lamp passes through a dark-field block, which consists of a light stop and ring mirrors to block the reflections, and is focused onto samples by a dark-field objective (numerical aperture, 0.8, ×50). The signal is collected by the same objective, and directed to a spectrometer.

The Raman spectroscopy is performed based on polarization-resolved Raman spectroscopy, which consists of the following components as shown in Supplementary Fig. 18b: 633-nm/532-nm continuous-wave lasers as pump sources; polarizers to set the linear polarization of incident light and measured signals; a motorized half-wave plate to tune the linear polarization of the pump; a quarter-wave plate with linear polarized light for the circular polarization; a long working distance objective (×40) with a numerical aperture of 0.6 (Nikon S plan) for microscopic imaging and micro-spectroscopy; a cryostat (Janis ST-500) to hold the sample at 77 K with liquid nitrogen flow; edge filters to remove any pump signals in the detection path; and the polarizer and half-wave plate in front of the spectrometer to analyse the emission polarizations. In the nonlinear power-law measurement, the pump is replaced by a tunable Ti:sapphire pulsed laser (Chameleon Ultra, 80 MHz repetition rate) with an optical parametric oscillator. In this case, the pump laser is narrowed to linewidth of 0.7 nm by a pair of clean-up filters. The motorized half-wave plate is used to automatically control the incident power. For all evaluation of optical helicity as well as the integral intensity of Raman modes, the background of the Raman spectrum is subtracted following an adaptive iteratively reweighted penalized least squares method[32], which is commonly used in spectral analysis, including Raman and surface-enhanced infrared absorption spectroscopy.

Simulation methods. The electromagnetic simulation is performed based on a commercial finite element methods software, COMSOL Multiphysics. The SHIN is modelled as a core–shell sphere and placed on a MoS_2 layer with a thickness of 1 nm, atop a 3-nm-Al_2O_3/500-nm-Au substrate. The size parameter of SHIN is set according to the TEM images and slightly adjusted to match the experimental data. The refractive index of SiO_2 is set to be constant at 1.4525; the complex index of MoS_2 is based on Supplementary Fig. 19; and the permittivity of gold and Al_2O_3 is adopted from a reference[33] and assumed to be independent of temperature. For CVD growth of the monolayer MoS_2, the dielectric function is described by superposed Lorentzian oscillators for excitons A and B. The excitonic energy, linewidth and oscillation strength parameters are evaluated from fitting the room temperature experimental reflectance spectrum for monolayer MoS_2 on Si/SiO_2 at normal incidence. Following a standard hyperbolic cotangent relation and a phenomenological description of phonon-induced broadening introduced by reference[34], the temperature-dependent excitonic energy and linewidth are obtained and applied to the Lorentzian model to derivate the dielectric function of CVD MoS_2 at cryogenic conditions.

To calculate the elastic scattering of SHIN, a scattering-field formulation is used, where the background field that exists in the absence of SHIN is defined analytically via evaluating reflections and transmissions at the interfaces. A perfect match layer was used to mimic the open boundaries. A finer mesh size of 0.5 nm was used around the SHIN.

Analysis of strong coupling regime by coupled-oscillator model. The strong coupling regime can be understood by a model of two coupled oscillators, where the excitons and plasmonic cavity modes are considered as two harmonic oscillators:

$$\begin{pmatrix} E_{ex}+i\Gamma_{ex} & V_A \\ V_A & E_{plm}+i\Gamma_{plm} \end{pmatrix}\begin{pmatrix}\alpha\\ \beta\end{pmatrix}=E\begin{pmatrix}\alpha\\ \beta\end{pmatrix}$$

Here the plasmonic cavity mode E_{plm} could vary with different sizes of the Au nanospheres. The exciton energy E_{ex} is set to be 1.865 eV from the differential reflectivity spectrum. The Γ_{plm} and Γ_{ex} are the half-width at half-maximum (HWHM) of the cavity photon and exciton, respectively. E are the eigenvalues corresponding to the energies of polariton modes. α and β construct the eigenvectors. V_A is the coupling strength. The eigenvalues E have two sets to represent the upper E_+ and lower E_- polariton branches:

$$E_\pm=\left(\frac{E_{ex}+E_{plm}}{2}\right)+i\left(\frac{\Gamma_{ex}+\Gamma_{plm}}{2}\right)\pm\sqrt{V_A^2+\frac{1}{4}(\delta+i\Gamma_{plm}-i\Gamma_{ex})^2}$$

where $\delta=E_{plm}-E_{ex}$ and $\hbar\Omega_{Rabi}=2\sqrt{V_A^2-\frac{1}{4}(\Gamma_{ex}-\Gamma_{plm})^2}$ (where ħ is the reduced Planck constant and Ω_{Rabi} is the Rabi frequency) is the Rabi splitting at detuning $\delta=0$. Note that α and β satisfying $|\alpha|^2+|\beta|^2=1$ also represent the Hopfield coefficients of the plasmonic cavity photon and exciton for each polariton state.

Based on the experimental data, the zero detuning $\delta=0$ can be directly recognized when $E_\pm$ have the same energy spacing from $E_{ex}=1.865$ eV with linewidth as the average of exciton and plasmon $\left(\frac{\Gamma_{ex}+\Gamma_{plm}}{2}\right)$. The HWHM of zero-detuned polaritons is 38 meV, and that of excitons is around 30 meV (Fig. 2a), while the HWHM of plasmons is estimated to be around 45 meV. Since the linewidth difference of a plasmon and exciton is very small (~15 meV), the Rabi splitting $\hbar\Omega_{Rabi}=2\sqrt{V_A^2-\frac{1}{4}(\Gamma_{ex}-\Gamma_{plm})^2}\approx 2V_A$ is estimated as 130 ± 6 meV based on measurement of more than ten zero-detuned cavity samples. The strong coupling regime requires $V_A^2>\frac{\Gamma_{ex}^2+\Gamma_{plm}^2}{2}$, which is fully satisfied in the systems studied based on these data. Together with this criterion, the features of the strong coupling regime in Fig. 2 are also similar to recent reports about the strong coupling regime of monolayer TMDs[35,36].

To fit the polariton states at non-zero detunings, the detuning δ cannot be directly obtained from experimental data. But δ can be either determined from estimated plasmon cavity resonance E_{plm} (based on the simulation method) or derived from this coupled-oscillator model. In this model, the upper and lower polariton separation ($\Delta E=E_+-E_-=\sqrt{4V_A^2+\delta^2}$) can be approximated as $\Delta E\cong 2V_A+\delta^2/4V_A$ when δ is small compared with $2V_A$. Thus δ can be derived from the energy spacing ΔE as $2V_A=130$ meV. The determination of δ from this model is valid for all the studied samples, and the polariton dispersion fits well with experimental data, as shown in Fig. 2c. Note here the plasmon cavity resonances E_{plm} from the detunings δ are also consistent with the estimated values based on the simulation of Supplementary Fig. 3.

Analysis of Raman modes. For the phonon scattering processes, classical Raman theory determines the Raman intensity I_0 for off-resonance scenarios as,

$$I_0\propto|\tilde{e_s}R\tilde{e_i}|^2 \quad (5)$$

where $\tilde{e_s}$, $\tilde{e_i}$ represent the electric field vectors of scattered and incident photons, respectively; R represents the Raman tensors of the modes.

The Raman tensors of the E′ and A_1' modes are given by,

$$R_{E'}=\begin{pmatrix}0&d&0\\ d&0&0\\ 0&0&0\end{pmatrix},\ R_{A_1'}=\begin{pmatrix}a&0&0\\ 0&a&0\\ 0&0&b\end{pmatrix}.$$

Here, *d*, *a* and *b* represent the elements in the Raman tensors in Cartesian coordinates. Based on the anisotropy of these Raman tensors, the E′ mode could rotate the linear polarization by 90° for the normal incidence of linearly polarized pump light along the *z* direction, while the A_1' mode could preserve the linear polarization. For circularly polarized pump light in the *z* direction, the vector is written as $\sigma\pm = \frac{1}{\sqrt{2}}\begin{pmatrix}1\\ \mp i\\ 0\end{pmatrix}$. The E′ mode could flip the handedness, and the A_1' mode could preserve the same handedness of the circular polarization. This is clearly observed in the plasmon case in Fig. 3, but does not apply any more when the exciton resonance comes into play, since the coupling of valley polarization becomes the dominant process.

Data availability

The data that support the findings of this study are available from the corresponding author upon reasonable request.

References

31. Li, J. F. et al. Surface analysis using shell-isolated nanoparticle-enhanced Raman spectroscopy. *Nat. Protoc.* **8**, 52–65 (2013).
32. Eilers, P. H. C. A perfect smoother. *Anal. Chem.* **75**, 3631–3636 (2003).
33. Palik, E. D. *Handbook of Optical Constants of Solids II* (Academic Press, 1991).
34. Cadiz, F. et al. Excitonic linewidth approaching the homogeneous limit in MoS_2-based van der Waals heterostructures. *Phys. Rev. X* **7**, 021026 (2017).
35. Kleemann, M. E. et al. Strong-coupling of WSe_2 in ultra-compact plasmonic nanocavities at room temperature. *Nat. Commun.* **8**, 1296 (2017).
36. Qin, J. et al. Revealing strong plasmon-exciton coupling between nanogap resonators and two-dimensional semiconductors at ambient conditions. *Phys. Rev. Lett.* **124**, 063902 (2020).

Acknowledgements

This work was supported by the King Abdullah University of Science and Technology Office of Sponsored Research award OSR-2016-CRG5-2996, National Science Foundation MRI grant 1725335 and the Ernest S. Kuh Endowed Chair Professorship. X.L. also acknowledges support from the National Natural Science Foundation of China (grant nos 12074297 and 62005202). J.-F.L. acknowledges support from National Natural Science Foundation of China (grant no. 21925404) and National Key Research and Development Program of China (2019YFA0705400). Y.-H.L. acknowledges support from the Ministry of Science and Technology (MoST 109-2124-M-007-001-MY3; 108-2112-M-007-006-MY3; 107-2923-M-007-002-MY3), the Frontier Research Center on Fundamental and Applied Sciences of Matters and the Center for Quantum Technology of National Tsing-Hua University.

Author contributions

X.L. and J.Y. conceived the ideas and designed the experiments. X.L., J.Y. and S.Y. conducted the experiments. J.Y. performed finite element methods simulations and the theoretical modelling. E.-C.L. and Y.-H.L synthesized the CVD monolayer MoS_2 sample. Y.-J.Z. and J.-F.L. synthesized the shell-isolated nanoparticles. X.Z. supervised the research. X.L. and J.Y. analysed the data and wrote the manuscript. All authors contributed to data interpretation and editing the manuscript.

Competing interests

The authors declare no competing interests.

Additional information

Supplementary information The online version contains supplementary material available at https://doi.org/10.1038/s41563-021-00972-x.

Correspondence and requests for materials should be addressed to X.Z.

Peer review information *Nature Materials* thanks Jeremy Baumberg and the other, anonymous, reviewer(s) for their contribution to the peer review of this work.

Reprints and permissions information is available at www.nature.com/reprints.